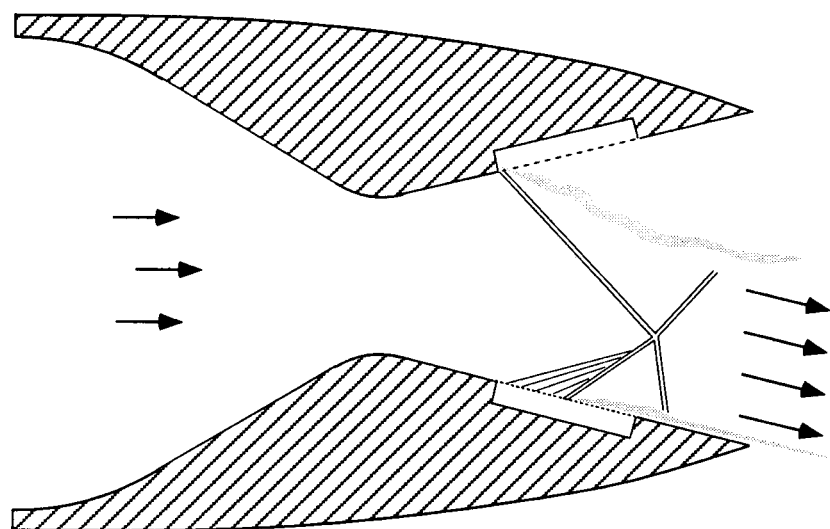# AIAA 96-2541

A Passive Cavity Concept for Improving the Off-Design Performance of Fixed-Geometry Exhaust Nozzles

Scott C. Asbury and Christopher L. Gunther
NASA Langley Research Center
Hampton, Virginia

Craig A. Hunter
The George Washington University JIAFS
NASA Langley Research Center
Hampton, Virginia

32nd AIAA/ASME/SAE/ASEE
Joint Propulsion Conference
July 1-3, 1996 / Lake Buena Vista, FL

A Passive Cavity Concept for Improving the Off-Design
Performance of Fixed-Geometry Exhaust Nozzles

Scott C. Asbury* and Christopher L. Gunther[†]
NASA Langley Research Center
Hampton, Virginia

Craig A. Hunter[‡]
The George Washington University JIAFS
NASA Langley Research Center
Hampton, Virginia

ABSTRACT

An investigation was conducted in the model preparation area of the Langley 16-Foot Transonic Tunnel to study a passive cavity concept for improving the off-design performance of fixed-geometry exhaust nozzles. Passive cavity ventilation (through a porous surface) was applied to divergent flap surfaces and tested at static conditions in a sub-scale, nonaxisymmetric, convergent-divergent nozzle. As part of a comprehensive investigation, force, moment and pressure measurements were taken and focusing schlieren flow visualization was obtained for a baseline configuration and 27 passive cavity configurations. All tests were conducted with no external flow and high-pressure air was used to simulate jet-exhaust flow at nozzle pressure ratios from 1.25 to approximately 9.50.

Results indicate that baseline nozzle performance was dominated by unstable shock-induced boundary-layer separation at off-design conditions, which came about through the natural tendency of overexpanded exhaust flow to satisfy conservation requirements by detaching from the nozzle divergent flaps. Passive cavity ventilation added the ability to control off-design separation in the nozzle by either alleviating separation or encouraging stable separation of the exhaust flow. Separation alleviation offers potential for installed nozzle performance benefits by reducing drag at forward flight speeds, even though it may reduce off-design static thrust efficiency as much as 3.2%. Encouraging stable separation of the exhaust flow offers significant performance improvements at static, low NPR and low Mach number flight conditions by improving off-design static thrust efficiency as much as 2.8%.

By designing a fixed-geometry nozzle with fully porous divergent flaps, where both cavity location and percent open porosity of the flaps could be varied, passive flow control would make it possible to improve off-design nozzle performance across a wide operating range. In addition, the ability to encourage separation on one flap while alleviating it on the other makes it possible to generate thrust vectoring in the nozzle through passive flow control.

---

* Aerospace Engineer, Component Integration Branch
† Cooperative Education Student, VPI&SU
‡ D.Sc. Candidate

INTRODUCTION

Supersonic cruise transport aircraft and modern military aircraft with supersonic cruise and dash capabilities utilize variable-geometry exhaust nozzles to ensure efficient operation across a wide speed range. A variable-geometry nozzle functions by mechanically adjusting throat area and exit area to provide the optimum nozzle expansion ratio for each throttle setting and flight condition. Nozzle geometry variation is typically performed using actuators and moveable nozzle flaps. While effective, these systems can be heavy, mechanically complex and prone to fatigue through thermal and aeroacoustic loading. In addition, variable-geometry mechanisms are inherently difficult to integrate into fighter aircraft afterbodies and can be a primary source of afterbody drag.

The desire for reduced cost, weight and complexity in exhaust systems has led designers to consider reducing, or even eliminating, the need for variable-geometry mechanisms in exhaust nozzles. The fundamental problem with this idea is that a fixed-geometry nozzle will only operate efficiently at the flight condition for which it is designed. When operated away from the design point (which may be common if a supersonic aircraft is expected to cruise subsonically, loiter, or divert to alternate airports), a fixed-geometry nozzle suffers serious off-design performance penalties.

Efficient operation of fixed-geometry nozzles across a large performance envelope will require the ability to control shock-induced boundary-layer separation at off-design conditions. At NPR's below that required for fully expanded flow (overexpanded), exhaust flow separation can improve static thrust efficiency by allowing a nozzle to adjust to an effectively lower expansion ratio. However, the stability of shock-induced separation is inherently unpredictable. Asymmetric, unsteady, or transitory separation can have a detrimental impact on nozzle performance and may result in undesirable flow vectoring, pressure pulsations and oscillatory flow inside the nozzle. Therefore, the ability to stabilize separation inside a fixed geometry nozzle is critical to efficient and practical off-design performance.

At forward flight speeds, external flow can aspirate the separated portion of the divergent flaps, causing increased drag and reduced thrust-minus-drag. In many instances, separation alleviation can improve aeropropulsive (thrust-minus-drag) performance, even if losses in static thrust efficiency occur from increased

exhaust flow overexpansion. Undoubtedly, a trade study would be required to determine the conditions a t which separation encouragement would be desirable or when separation alleviation would be most beneficial to nozzle aeropropulsive performance.

NOMENCLATURE

A_e	nozzle exit area, 7.758 in^2
A_t	nozzle throat area, 4.317 in^2
$C_{F,\eta}$	thrust efficiency coefficient, F/F_i
$(C_{F,\eta})_{peak}$	peak thrust efficiency
D	passive cavity depth, in.
d	porous plate hole diameter, in.
F	measured axial thrust, lbf
F_i	ideal isentropic thrust, lbf
M_1	Mach number just upstream of a shock
NPR	nozzle pressure ratio, $p_{t,j}/p_a$
NPR$_d$	design NPR (fully expanded flow)
p	local static pressure, psi
p_a	ambient pressure, psi
$p_{t,j}$	average jet total pressure, psi
Sta.	model station, in.
x,y,z	nozzle coordinates, in.
x_t	nozzle throat location, 2.275 in.

NOZZLE CONCEPTS

A fixed-geometry, nonaxisymmetric nozzle was designed with symmetric pairs (upper and lower) of convergent and divergent flaps and sidewalls to contain exhaust flow in the lateral direction. In an attempt to control off-design separation in the nozzle, the baseline design was modified by adding a passive cavity ventilated through a porous surface to each divergent flap.

Passive Cavity Ventilation

Figure 1 illustrates the passive cavity concept for shock-boundary layer interaction control[1]. This concept consists of a porous surface and passive cavity located in the shock-boundary layer interaction region. As shown in figure 1, high pressure downstream of the shock induces flow into the cavity, which exits into the low pressure region upstream of the shock, producing an upstream blowing/downstream suction flow. The porosity of the porous surface is typically kept low to minimize cavity flows and associated effects under conditions when a shock is not present over the passive cavity.

In terms of separation alleviation, the passive cavity functions in several ways. First, upstream blowing results in increased pressure communication and generates weak oblique waves ahead of the main shock, extending the shock-boundary layer interaction region further upstream. This results in a more

gradual, more isentropic pressure rise, a weaker shock system, and reduces the tendency for shock-induced boundary layer separation to occur[2]. In addition, suction downstream of the shock suppresses boundary layer detachment, closing down possible separation regions and damping out unsteady effects of the shock-boundary layer interaction[1].

In terms of separation encouragement, this report will demonstrate that the blowing/suction mechanism can actually become too strong and disturb nozzle flow. When this occurs, a large separation region forms on the divergent flaps and encourages stable separation of the exhaust flow.

NOZZLE MODELS

Nozzle Test bed

The model used in this investigation was a sub-scale, nonaxisymmetric, convergent-divergent nozzle with an expansion ratio (A_e/A_t) of 1.797 (NPR$_d$=8.78), a nominal throat area (A_t) of 4.317 in^2 and a constant flow path width of 3.990 in. A photograph of the nozzle model with baseline flap inserts installed is presented in figure 2. A sketch of the nozzle model and a geometric definition of the nozzle internal flowpath with baseline flap inserts installed are presented in figure 3.

The basic model was composed of two nozzle flap assemblies, capable of accepting interchangeable divergent-flap inserts, and two sidewall assemblies, which had optical quality boro-silicate crown glass windows for internal focusing schlieren flow visualization.

The model was designed with twenty-eight pairs of interchangeable divergent flap inserts such that the effects of divergent flap modifications on shock-boundary layer interaction control and nozzle performance could be determined. Inserts tested included a baseline configuration (shown installed in figure 3) and 27 passive cavity configurations (fig. 4). An additional configuration was also tested that combined a passive cavity insert that encouraged separation installed in the upper flap and a baseline insert installed in the lower flap in a attempt to generate thrust vectoring through passive flow control.

Passive cavity configurations

Details of passive cavity flap inserts are presented in figure 4. Shallow, medium and deep cavity depths were tested. Porous plate hole diameter variations were 0.025 in., 0.052 in. and 0.076 in. Plate porosity variations were 10%, 20% and 30% open. Variations in cavity depth, porous plate hole diameter and plate porosity combined to provide 27 passive cavity configurations.

APPARATUS AND PROCEDURE

Test Facility

This investigation was conducted in the model preparation area of the Langley 16-Foot Transonic Tunnel. Although this area is normally used for setup and calibration of wind-tunnel models, it can also be used for nozzle internal performance testing at static conditions. Testing is conducted in a 10 x 29 foot chamber where the jet from a sting-strut supported single-engine propulsion simulation system exhausts to the atmosphere through an acoustically treated exhaust passage. A control room is adjacent to the test chamber, and offers access through a sound-proof door and observation window. The model preparation area shares an air supply system with the 16-Foot Transonic Tunnel that includes valving, filters and a heat exchanger to provide a continuous flow of clean, dry air to the propulsion simulation system. A complete description of the test facility is provided in reference 3.

Single-Engine Propulsion Simulation System

High-pressure air was supplied to the propulsion simulation system (fig. 5) at a constant stagnation temperature of about 540°R at the nozzle. As shown in figure 6, the high-pressure air supply was delivered by six air lines through a support strut into an annular high-pressure plenum. The air was then discharged radially into a low-pressure plenum through eight equally spaced, multiholed sonic nozzles. This flow transfer system was designed to minimize any forces imposed by the transfer of axial momentum as the air passed from the non-metric high-pressure plenum to the metric (attached to the balance) low-pressure plenum. Two flexible metal bellows functioned as seals between the non-metric and metric portions of the model and compensated for axial forces caused by pressurization. The air then passed through a circular-to-rectangular transition section, a choke plate, an instrumentation section and the nozzle, which exhausted to atmospheric back pressure.

Instrumentation

The weight-flow rate of high-pressure air supplied to the nozzle was calculated from pressure and temperature measurements in a calibrated multiple-critical venturi system located upstream of the propulsion simulation system. Forces and moments generated by the nozzle were measured by a six-component strain-gauge balance located on the centerline of the propulsion simulation system (fig. 6). Jet total pressure was measured at a fixed station in the instrumentation section with a four-probe rake through the upper surface and a three-probe rake through the corner. Jet total temperature was measured in the instrumentation section by two iron-constantan thermocouples.

Internal static pressure distributions were measured along the upper flap for each configuration. Common to all configurations were six static pressure orifices in the convergent section and one orifice at the geometric throat, all located on the nozzle centerline (z=0.000 in.). Each upper flap insert was equipped with a row of centerline (z=0.000 in.) and sideline (z=1.595 in.) pressure orifices. In addition, passive cavity configurations contained static pressure orifices located on the bottom of the passive cavity near the nozzle centerline at z=-0.200 in.

Data Reduction

Fifty frames of data, taken at a rate of 10 frames per second, were averaged for each measured data parameter. Calibration constants were applied to the data to obtain corrected forces, moments, pressures and temperatures. A detailed description of the procedures used for data reduction in this investigation can be found in reference 4.

Nozzle pressure ratio is the average jet total pressure $p_{t,j}$ measured in the instrumentation section divided by ambient pressure p_a and was varied in this investigation from 1.25 to approximately 9.50. Nozzle thrust efficiency $C_{F,\eta}$ is the ratio of measured axial thrust F to the ideal isentropic thrust F_i, which is calculated using the measured weight-flow rate, total pressure and total temperature of the jet.

Focusing Schlieren Flow Visualization

A focusing schlieren flow visualization system was used during this investigation to visualize nozzle exhaust flow. The system was built based on criterion reported in reference 5. The system was characterized by a 133 mm diameter field of view, a sensitivity of 17 arcsec, a resolution of 0.25 mm, a depth of sharp focus of 4.6 mm and a depth of unsharp focus of 36 mm.

The light source for the focusing schlieren system was a xenon strobe flash tube. A driving circuit picked up sync pulses generated by a recording video camera and triggered the flash at a 30 Hz rate with pulses of 0.6 μsec duration and 0.05 watt-sec power. Along with a 720 x 480 pixel resolution video camera, a 70 mm Hasselblad still camera recorded results.

The focusing schlieren system was assembled on a 44 x 66 inch table that mounted on a rigid platform equipped with casters and leveling screws. The platform was placed under the propulsion simulation system and jacked and leveled into position. The compactness of the system allowed flow visualization to be recorded simultaneously with data acquisition.

RESULTS AND DISCUSSION

Baseline Configuration

On-design performance. Nozzle thrust efficiency $C_{F,\eta}$ for the baseline configuration is presented as a function of nozzle pressure ratio (NPR) in figure 7. The baseline configuration experienced peak thrust efficiency $(C_F,\eta)_{peak}$ of 0.986 near the design NPR (NPR_d) of 8.78 which was within the 0.985 to 0.990 range typical of nonaxisymmetric, convergent-divergent nozzles[6-8]. The approximate 1.4% loss in peak thrust efficiency near NPR_d can be attributed to exit-flow angularity effects and friction drag inside the nozzle.

Off-design performance. Nozzle thrust efficiency tapered off slowly below NPR_d as the result of exhaust flow overexpansion effects (fig. 7). Internal static pressure distributions for the baseline configuration are presented in figure 8, normalized by jet total pressure $p_{t,j}$ and plotted against nondimensionalized streamwise location relative to the nozzle throat, x/x_t. These distributions are typical of convergent-divergent nozzle flow characteristics[9]. For centerline pressures ($z=0.000$ in.), the first two curves at NPR's of 1.25 and 1.4 indicate choked ($p/p_{t,j} \leq 0.528$), internally overexpanded flow with a weak shock present near the nozzle geometric throat ($x/x_t=1.0$). Flow downstream of the shock remained attached and recovered to ambient pressure ($p/p_{t,j}=1/NPR$) in a smooth, continuous fashion. Flow visualization for the baseline configuration at NPR=1.4 in figure 9(a) shows a weak, almost normal shock downstream of the throat with little or no lambda foot structure evident. This behavior is characteristic of a weak shock with a flow Mach number of approximately 1.2 just upstream of the shock (M_1) and a thin boundary layer inside the nozzle. Note that flow Mach number inside the nozzle was estimated from $p/p_{t,j}$.

As shown in figure 8, the discontinuous nature of the centerline pressure distribution at NPR=1.6 indicates that shock strength increased ($M_1 \approx 1.4$) and the inflection point in the pressure recovery downstream of the shock at $x/x_t \approx 1.25$ indicates that flow separation occurred on the divergent flaps, though it was not severe. By NPR=1.8, the upstream shock Mach number was $M_1 \approx 1.5$ and shock-induced boundary-layer separation began to dominate nozzle flow characteristics. At NPR=1.8, there are strong signs of a separation bubble, with minimal pressure recovery indicated by a relatively flat pressure distribution from the shock location at $x/x_t \approx 1.3$ out to $x/x_t \approx 1.6$; however, full recovery to ambient pressure occurred over the remaining length of the nozzle. Flow visualization at NPR=1.8 in figure 9(b) shows the shock with a small lambda foot structure. Highly

unstable flow is also indicated, as the schlieren photograph imaged the shock in two positions over a 0.6 μsec duration.

An increase in pressure ratio to NPR=2.0 did not significantly change shock location or strength, but resulted in fully detached shock-induced separation with almost no pressure recovery downstream of the shock (fig. 8). Flow visualization at NPR=2.0 in figure 9(c) shows the shock with a pronounced lambda foot structure. These results indicate that the nozzle flow adjusted to exit conditions at NPR=2.0 simply by separating from the divergent flaps, while normalized pressure (and thus Mach number) upstream of the shock matched those of the previous NPR. This behavior indicates that the onset of full separation at NPR=2.0 was not the result of a stronger shock-boundary layer interaction, but instead came about through the natural tendency of overexpanded exhaust flow to conserve mass, momentum and energy by detaching from the divergent flaps and adjusting to an effectively shorter, smaller, lower expansion ratio nozzle. Not surprisingly, overexpansion losses decreased as a result of this mechanism and there was a marked increase in static thrust efficiency at NPR=2.0 (fig. 7).

As shown in figure 8, fully detached separation occurred for all subsequent internally overexpanded NPR's above 2.0. Increasing NPR beyond 2.0 moved the shock farther down the nozzle until it was positioned near the exit at NPR=5.0. At NPR=5.4, the shock moved out of the nozzle which then became internally shock free. As a result, all pressure distributions fell on the same curve and internal flow characteristics were independent of NPR beyond that point.

Passive Cavity Configurations

On-design performance. To determine peak thrust efficiency trends for passive cavity configurations, a "response plot" was generated for each cavity depth by plotting $(C_F,\eta)_{peak}$ against hole diameter d and percent porosity in figure 10. Peak thrust efficiencies for passive cavity configurations were all slightly lower than the baseline $(C_F,\eta)_{peak}$ of 0.986, ranging from a low of 0.980 to a high of 0.985. Each response plot shows a general trend of peak thrust efficiency decreasing with increasing porosity and decreasing hole diameter. Likely causes of this trend are increased surface roughness of the porous plates and passive cavity flow effects.

Effect of surface roughness. Surface roughness of the porous plates is dependent on both hole diameter and percent porosity. For a fixed hole diameter, increasing porosity resulted in more holes and greater effective surface roughness. Likewise, for a fixed porosity, reducing hole diameter also resulted

4

in more holes and greater effective surface roughness. In either case, greater effective surface roughness increased nozzle skin friction drag and reduced nozzle thrust efficiency.

Effect of passive cavity flow. Passive cavity flow was also dependent on hole diameter and percent porosity, since this effect was governed by an upstream blowing/downstream suction mechanism that induced flow through the porous plate. Given the fact that boundary layer displacement thickness was significantly thinner than even the smallest porous plate hole diameter investigated, it is unlikely that boundary layer-hole diameter scaling had any effect on cavity flow for the range of hole diameters tested. Therefore, an increase in the open area distribution, due to reduced hole diameter or higher porosity, resulted in increased cavity flow. At on-design conditions, flow through the cavity would generate high pressures on the rearward-facing front step and low pressures on the forward-facing aft step. As a result, cavity pressures generated an internal drag and reduced nozzle thrust efficiency.

Off-design performance. Passive cavity ventilation added the ability to control off-design separation in the nozzle, by either alleviating separation or encouraging stable separation of the exhaust flow. Data for selected configurations will be presented and used to discuss representative results for each category.

Separation alleviation. Passive cavity configurations with low porosity and large hole diameter generally reduced off-design nozzle performance relative to the baseline configuration, indicating that they were most effective at alleviating separation. To better understand this behavior, performance of the passive cavity configuration with 10% porosity, $d=0.076$ in. and a deep cavity is examined. As shown in figure 11, this configuration had lower $C_{F,\eta}$ than the baseline configuration across the entire NPR range investigated. Static pressure distributions for this configuration are presented in figure 12 for each NPR tested. For NPR's up to 1.6, flow characteristics were similar to the partially separated baseline configuration (fig. 8) and the shock was positioned upstream of the passive cavity. However, thrust efficiency was as much as 3.2% lower for the passive cavity configuration at these NPR's (fig. 11), indicating that the passive cavity may have been providing some separation alleviation downstream of the shock in the divergent section of the nozzle. Surface and cavity pressures for NPR's up to 1.61 are compared in figure 13. Relative to surface pressures, low pressure in the downstream end of the cavity and high pressure in the upstream end of the cavity suggests that there was upstream flow out of the cavity and downstream flow into the cavity, or

upstream blowing/downstream suction. Thus, an entrainment mechanism may have reduced separation simply by pulling the exhaust flow towards the divergent flaps along the downstream portion of the passive cavity. Reduced separation in the nozzle would increase losses due to exhaust flow overexpansion and cause the reduction in $C_{F,\eta}$ (relative to the baseline configuration) shown in figure 11.

As NPR was increased to 1.8, the shock moved to the leading edge of the passive cavity (fig. 12) and compression through the shock was gradual. The inflection point in the pressure recovery curve at the leading edge of the passive cavity indicates that there was some separation downstream of the shock. Flow visualization at NPR=1.8 in figure 14(a) shows the shock with a large, disorganized, apparently unstable lambda foot structure. It wasn't until NPR=2.0 that the shock moved over the passive cavity (fig. 12) and the shock structure was better defined. Flow visualization at NPR=2.0 in figure 14(b) shows that, on each divergent flap, an oblique wave emanated from each of the two rows of porous plate holes upstream of the shock. These waves intersected the main shock, which had a small, undefined lambda foot structure. Past the compression region, pressure data show that the inflection point in the pressure recovery curve was nearly gone and that complete recovery to ambient pressure occurred.

A comparison of surface and cavity internal static pressure distributions for this configuration at NPR's from 1.81 to 3.01 is presented in figure 15. Again, pressure distributions inside the passive cavity at NPR's up to 2.6 suggest that there was upstream flow out of the cavity and downstream flow into the cavity, or upstream blowing/downstream suction. Flow visualization at NPR=2.4 in figure 16(a) shows oblique waves emanating from the upstream end of the passive cavity. When coupled with pressure data, this suggests that the passive cavity was functioning as intended, by communicating the shock jump condition and its associated pressure rise upstream through the blowing/suction mechanism. Upstream blowing generated weak compression waves ahead of the main shock, spreading the shock pressure rise over a longer distance and downstream suction closed the separation region behind the shock. Compared to the baseline case, this resulted in a more gradual compression through the main shock, effectively alleviating separation and providing good downstream pressure recovery.

By NPR=3.0, pressure data in figure 12 show that the leading lambda foot was near the very end of the passive cavity; cavity pressures flattened out and were higher than surface pressures near the downstream end of the cavity (fig. 15). This indicates that blowing/suction flow in the passive cavity was

significantly reduced, eliminated, or had possibly even reversed to transitional-closed cavity flow[10]. In this type of flow, flows over the front and rear of the cavity are similar to supersonic flows over rearward- and forward-facing steps, respectively, and result in low pressures acting on the rearward-facing front step and high pressures acting on the forward-facing aft step. As a result, cavity pressures would act to generate an internal drag and reduce nozzle thrust efficiency. Accordingly, flow visualization at NPR=3.0 in figure 16(b) shows that the oblique waves seen at previous NPR's had vanished and were replaced by Mach lines.

Beyond NPR=3.0, the passive cavity provided little separation alleviation and static pressure distributions resembled those of the baseline configuration (fig. 8). Losses in $C_{F,\eta}$ above NPR=3.0 are likely the result of internal drag generated by transitional-closed cavity flow. Static pressure data in figure 12 show that the shock moved smoothly out of the nozzle, which was internally shock free at NPR's above 5.4.

Passive cavity configurations that alleviated off-design separation also had higher on-design peak thrust efficiency than other passive cavity configurations, with $(C_{F,\eta})_{peak}$ ranging from only 0.2% to 0.3% below baseline. Both off-design separation alleviation and low on-design losses can be attributed to minimized cavity entrainment for these configurations. At off-design conditions, the passive cavity functioned by producing a blowing/suction mechanism that spread the shock jump over a longer distance and closed down the separation region behind the shock. At on-design conditions, minimal cavity entrainment limited drag generating transitional-closed cavity flow.

Separation encouragement. Passive cavity configurations with high porosity and small hole diameter generally improved off-design nozzle performance, suggesting that these configurations encouraged exhaust flow separation. As shown in figure 17, the passive cavity configuration with 20% porosity, d=0.025 in. and a shallow cavity had $C_{F,\eta}$ as much as 1.5% higher than the baseline configuration over an extended NPR range between 2.0 and 4.0. Static pressure distributions for this configuration are presented in figure 18 for each NPR tested. For NPR's up to 1.6, pressure distributions show that flow characteristics were similar to the partially separated baseline configuration (fig. 8) and the shock was positioned upstream of the passive cavity. Relative to the previously discussed passive cavity configuration, low NPR thrust efficiency for this configuration was higher and closer to baseline levels.

A comparison of surface and cavity internal static pressure distributions for this configuration in figure 19 shows nearly equal pressures at NPR's from 1.25 to 1.60, indicating that there was no blowing/suction mechanism at these low NPR's. This was surprising, since this configuration had a significantly greater open area than the previously discussed configuration and was expected to have increased cavity entrainment and better separation alleviation. This may simply indicate that increased cavity entrainment coupled with the separation to form a recirculation region on the divergent flap. As a result, low NPR thrust efficiency for this configuration was higher and closer to baseline levels than the previously discussed configuration.

At NPR=1.8, the shock moved to the beginning of the passive cavity and remained fixed at that location for five subsequent NPR's (fig. 18). As a result, compression through the shock became more and more gradual as NPR increased and downstream pressure recovery flattened out considerably. Flow visualization at NPR's of 1.8 and 2.6 in figure 20 shows that as NPR increased, the leading branch of the lambda foot remained at the start of the passive cavity while the main portion of the shock moved downstream. In each case, flow separated past the leading lambda foot (fig. 18) and by NPR=2.6, flow inside the nozzle resembled flow downstream of the exit of a typical overexpanded nozzle; the bifurcation point of the lambda foot was near the nozzle centerline and the internal shock system took the form of the first shock cell downstream of the exit of a highly overexpanded, shorter, lower expansion ratio nozzle. There was an expansion fan past each trailing lambda foot and an external shock cell was visible within the field of view of the schlieren system, downstream of the physical nozzle exit. Pressure data at NPR=2.6 in figure 18 show that pressures were nearly constant over the entire length of the divergent flap.

These results indicate that this configuration didn't alleviate separation, but instead "encouraged" nozzle separation, such that the mutually dependent shock location-separation condition resulted in a drastic change in the effective nozzle geometry. This is especially evident in thrust efficiency data presented in figure 17, which showed a steady increase in $C_{F,\eta}$ over the baseline value from NPR's of 2.0 to 2.6, at which point this configuration had a thrust efficiency of 0.927, 1.4% higher than baseline. The reasons for such behavior are not immediately evident, but it is obvious that with a fixed leading lambda foot, onset shock-boundary layer interaction conditions were virtually the same at NPR's from 2.0 to 2.6. In addition, the nozzle geometry up to the shock location was the same in this configuration as in the baseline configuration, indicating that conditions downstream of the shock drove the shock-boundary layer interaction.

Surface and cavity internal static pressure distributions for this configuration are compared at

6

NPR's from 2.0 to 3.0 in figure 21 and show virtually no difference and near constant pressures across the passive cavity. This suggests that the passive cavity vented the nozzle flap to a constant pressure and encouraged the natural tendency of the exhaust flow to separate from the divergent flaps. This fixed the nozzle exit at the furthest upstream ventilated point, stabilized separation, lowered the effective expansion ratio of the nozzle and improved performance. Given that this configuration differed from the previously discussed configuration in its smaller hole diameter and higher porosity, this upstream ventilation mechanism can be attributed to increased cavity flow. Combined with the behavior observed at lower NPR's, this suggests that there was a point (i.e., porosity, hole diameter) at which the blowing/suction mechanism of the passive cavity became too strong and disturbed nozzle flow, setting up a large recirculating region on the divergent flap.

An increase in NPR to 3.0 did not push the shock cell downstream, but the shock instead reformed at the trailing edge of the passive cavity with a lambda foot, as shown in figure 22. Pressure data in figure 18 show that flow partially expanded across the passive cavity and began to resemble transitional-closed cavity flow. It is apparent that in raising NPR from 2.6 to 3.0, the increase in nozzle pressure ratio was enough to overcome the ventilation mechanism of the passive cavity and move the shock downstream. With the end of separation and the beginning of closed cavity flow, thrust efficiency began to decrease back towards the baseline value (fig. 17).

Static pressure distributions in figure 18 show that the passive cavity continued to affect internal flow characteristics at NPR's up to 4.2, but by NPR=4.6, the shock was well downstream of the passive cavity. Static pressure distributions in figure 18 show that the shock moved smoothly out of the nozzle, which was internally shock free at NPR's above 5.4.

Effect of cavity depth. In general, the effects of cavity depth were smaller than the effects of either porosity or hole diameter discussed previously. The most significant effects of cavity depth occurred at the smallest hole diameter tested, while configurations with larger hole diameters showed little or no effect of cavity depth on performance.

Figure 23(a) presents the effects of cavity depth on performance of passive cavity configurations with 10% porosity and d=0.025 in. The data shows an extended NPR range where $C_{F,\eta}$ for the deep cavity configuration was significantly higher than the baseline nozzle, rising above the baseline value as much as 2.8% at NPR=2.6. This indicates that this configuration was most effective at encouraging separation, suggesting a 3-way interaction between

porosity, hole diameter and cavity depth that combined to produce the largest amount of cavity flow for any of the passive cavity configurations.

This behavior did not continue at higher porosities for configurations with the smallest hole diameter. As shown in figures 23(b) and 23(c), there was a reversal in the off-design performance trend as cavity depth was increased to a maximum. This indicates a weakening of cavity flow at the deepest cavity depth for these configurations.

Passive Flow Control

Passive cavity configurations that alleviated shock-induced boundary-layer separation can potentially improve aeropropulsive performance of installed exhaust nozzles with little or no on-design performance penalties. Configurations that encourage separation can improve off-design thrust efficiency at static, low NPR and low Mach number flight conditions such as takeoff and landing. Together, the ability to either alleviate or encourage separation in fixed-geometry nozzles offers tremendous potential to passively or semi-actively control nozzle flows. By designing a fixed-geometry nozzle with fully porous divergent flaps, where both the cavity location and percent porosity of the flaps could be controlled, the passive cavity concept can produce thrust vectoring as shown in figure 24. In this application, sliding porous plates control the passive cavity geometry and encourage separation on the upper divergent flap, while alleviating separation on the lower flap. Flow visualization at NPR=2.0 in figure 25 shows the results of testing a configuration which encouraged separation on the upper flap (10% porosity, d = 0.025 in. and deep cavity), while flow remained attached on the lower flap where a baseline insert was installed. This photograph clearly shows the thrust vectoring capability of the passive cavity nozzle concept, which generated 11° of pitch vectoring through passive flow control.

CONCLUSIONS

An investigation was conducted in the model preparation area of the Langley 16-Foot Transonic Tunnel to study a passive cavity concept for improving the off-design performance of fixed-geometry exhaust nozzles. Passive cavity ventilation (through a porous surface) was applied to divergent flap surfaces and tested at static conditions in a sub-scale, nonaxisymmetric, convergent-divergent nozzle. As part of a comprehensive investigation, force, moment and pressure measurements were taken and focusing schlieren flow visualization was obtained for a baseline configuration and 27 passive cavity configurations. All tests were conducted with no

external flow and nozzle pressure ratio was varied during jet simulation from 1.25 to approximately 9.50. The results of this investigation indicate the following conclusions:

1. Baseline nozzle performance was dominated by the effects of fully detached, shock-induced boundary-layer separation that was highly unstable. This separation came about through the natural tendency of overexpanded exhaust flow to satisfy conservation requirements by detaching from the nozzle divergent flaps and adjusting to an effectively lower expansion ratio nozzle.

2. Passive cavity ventilation added the ability to control off-design separation in the nozzle by either alleviating separation or encouraging stable separation of the exhaust flow. Separation alleviation offers potential for installed nozzle performance benefits by reducing drag at forward flight speeds, even though it may reduce off-design static thrust efficiency as much as 3.2%. Encouraging stable separation of the exhaust flow offers significant performance improvements at static, low NPR and low Mach number flight conditions by improving off-design static thrust efficiency as much as 2.8%.

3. The ability to alleviate or encourage stable separation through passive flow control offers tremendous off-design performance benefits for fixed-geometry nozzle installations. By designing a fixed-geometry nozzle with fully porous divergent flaps, where both cavity location and percent open porosity could be varied, passive flow control would make it possible to improve off-design nozzle performance across a wide operating range. In addition, the ability to encourage separation on one flap while alleviating separation on the other, makes it possible to generate thrust vectoring in a fixed-geometry nozzle through passive flow control.

REFERENCES

1. Raghunathan, S.: Passive Control of Shock-Boundary Layer Interaction. *Progress in Aerospace Sciences*, vol. 25, 1988.

2. McCormick, D.C.: Shock-Boundary Layer Interaction Control with Low-Profile Vortex Generators and Passive Cavity. AIAA-92-0064, January 1992.

3. Staff of the Propulsion Aerodynamics Branch: *A User's Guide to the Langley 16-Foot Transonic Tunnel Complex, Revision 1*. NASA TM-102750, 1990. (Supersedes NASA TM-83186, compiled by Kathryn H. Peddrew, 1981.)

4. Mercer, Charles E.; Berrier, Bobby L.; Capone, Francis J.; and Grayston, Alan M.: *Data Reduction Formulas for the 16-Foot Transonic Tunnel–NASA Langley Research Center. Revision 2*. NASA TM-107646, 1992.

5. Weinstein, L.M.: An Improved Large-Field Focusing Schlieren System. AIAA-91-0567, January 1991.

6. Capone, F.J.; Konarski, M.; Stevens, H.L.; and Willard, C.M.: Static Performance of Vectoring/Reversing Non-Axisymmetric Nozzles. AIAA-77-840, July 1977.

7. Re, Richard J.; and Leavitt, Laurence D.: *Static Internal Performance Including Thrust Vectoring and Thrust Reversing of Two-Dimensional Convergent-Divergent Nozzles*. NASA TP-2253, 1984.

8. Taylor, John G.: *Static Investigation of a Two-Dimensional Convergent Divergent Exhaust Nozzle With Multiaxis Thrust Vectoring Capability*. NASA TP-2973, 1990.

9. Liepmann, Hans Wolfgang; and Roshko, Anatol: *Elements of Gasdynamics*. John Wiley & Sons, Inc., 1957.

10. Stallings, R.L., Jr.; and Wilcox, F.J., Jr.: *Experimental Cavity Pressure Distributions at Supersonic Speeds*. NASA TP-2683, 1987.
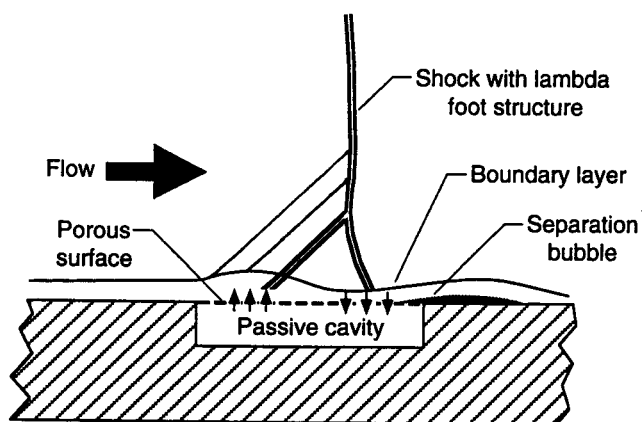
Fig. 1 Sketch showing passive cavity concept for shock-boundary layer interaction control.

Fig. 2 Photograph of nozzle model with baseline flap inserts installed.

Point	Cooridinates, in.	
	x	y
1	0.000	0.000
2	0.000	-0.614
3	0.000	1.386
4	0.917	1.163
5	1.988	0.611
6	2.394	0.553
7	2.430	0.559
8	2.275	1.166
9	4.550	0.972
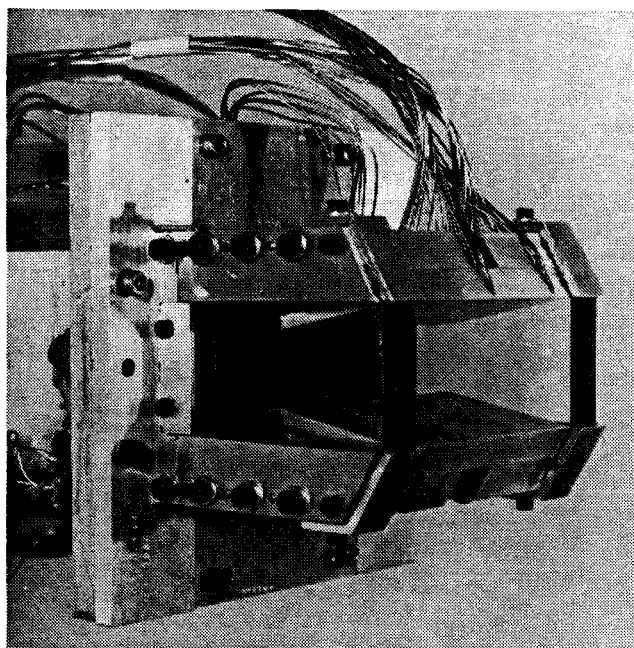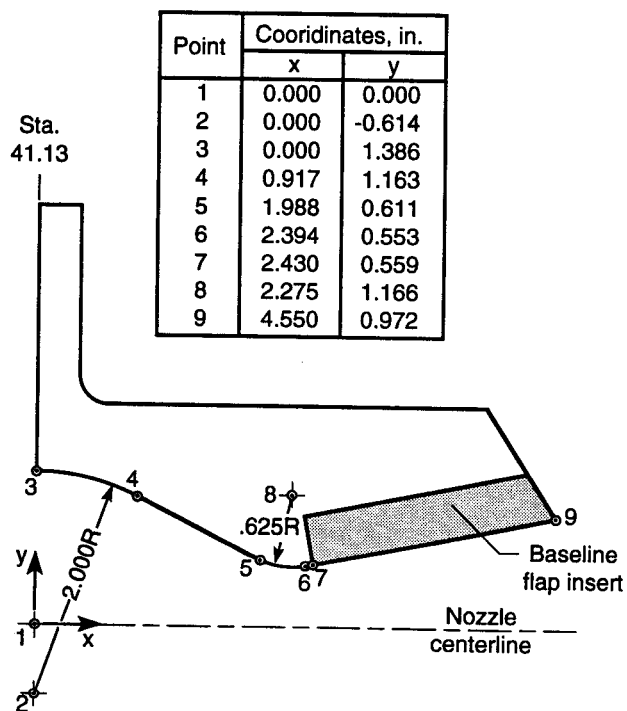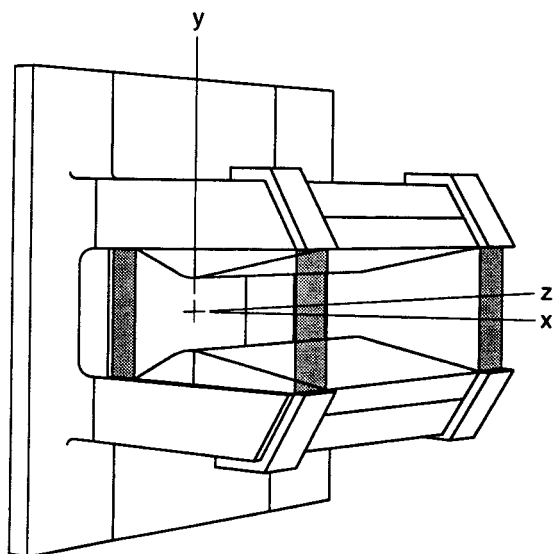
Fig. 3 Sketch of nozzle model and geometric definition of internal flowpath with baseline flap inserts installed.

Top view

2.160

3.990

Side view

.500 1.000 .660 .031

D .500
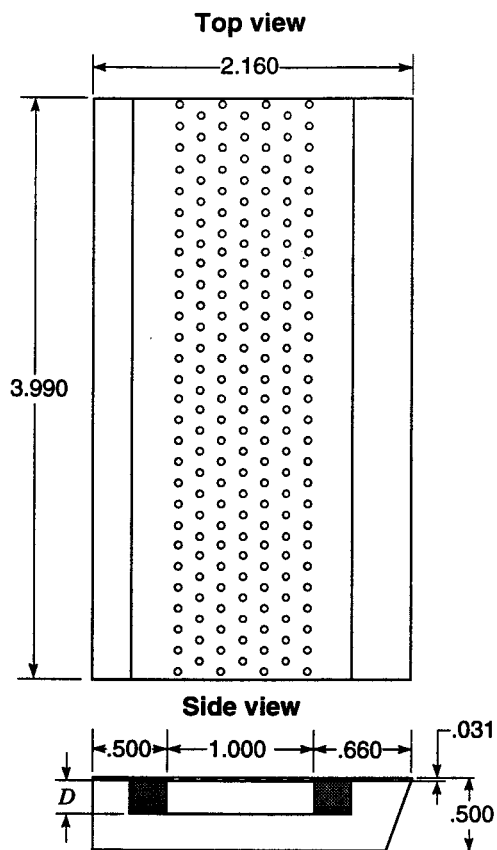
Passive cavity configuration test matrix

Hole diameter d, in.

0.025 0.052 0.076

0.072 0.119 0.219
0.040 0.087 0.187
0.040 0.087 0.187

Shallow Medium Deep

Cavity depth D, in.

10 20 30

Porosity, %
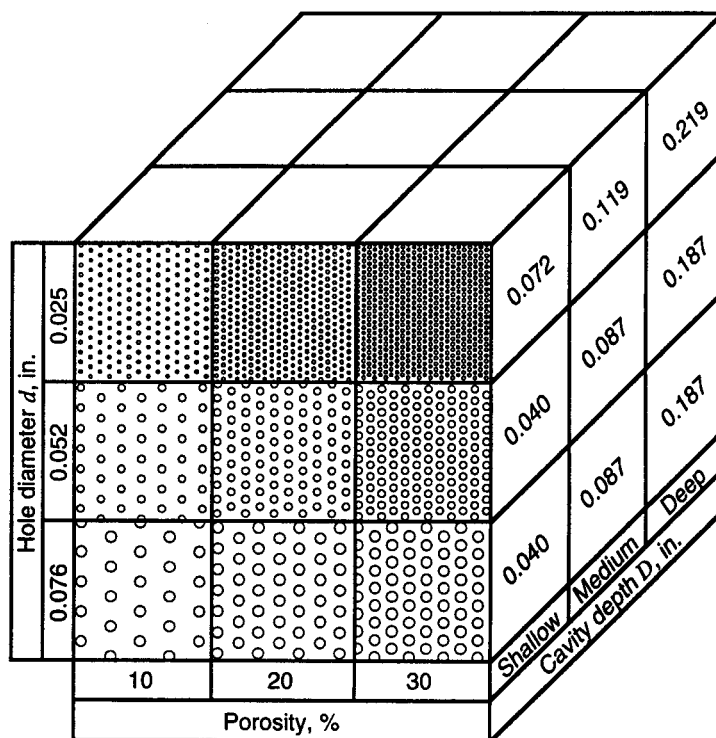
Photograph of nozzle model with passive cavity flap inserts installed
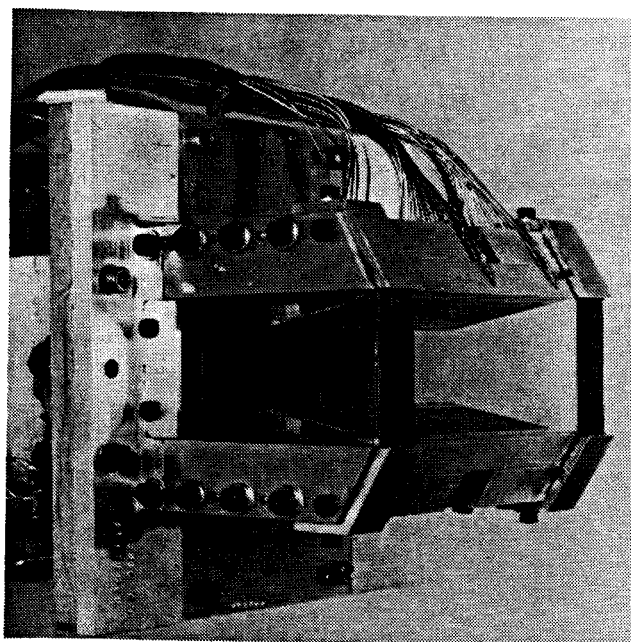
Fig. 4 Details of passive cavity flap inserts. All dimensions are in inches.
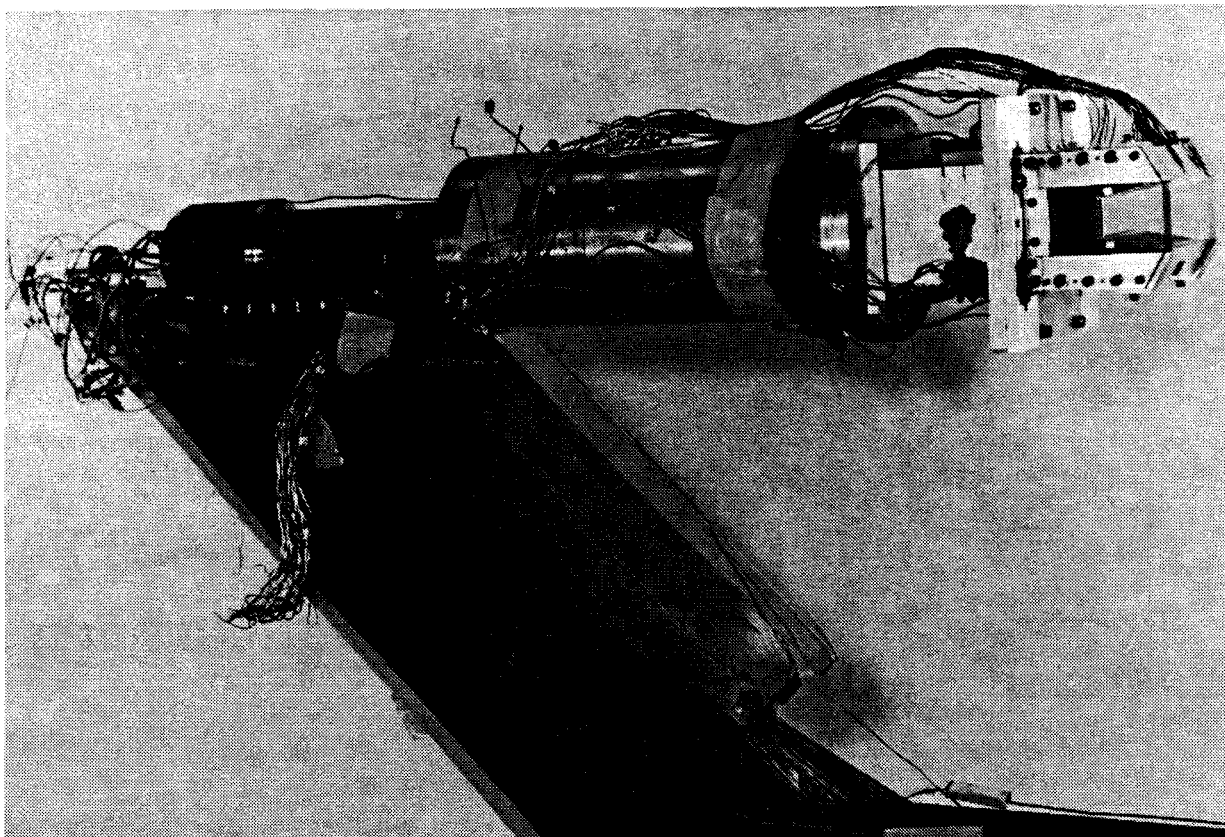
Fig. 5 Photograph of nozzle model installed on the propulsion simulation system.
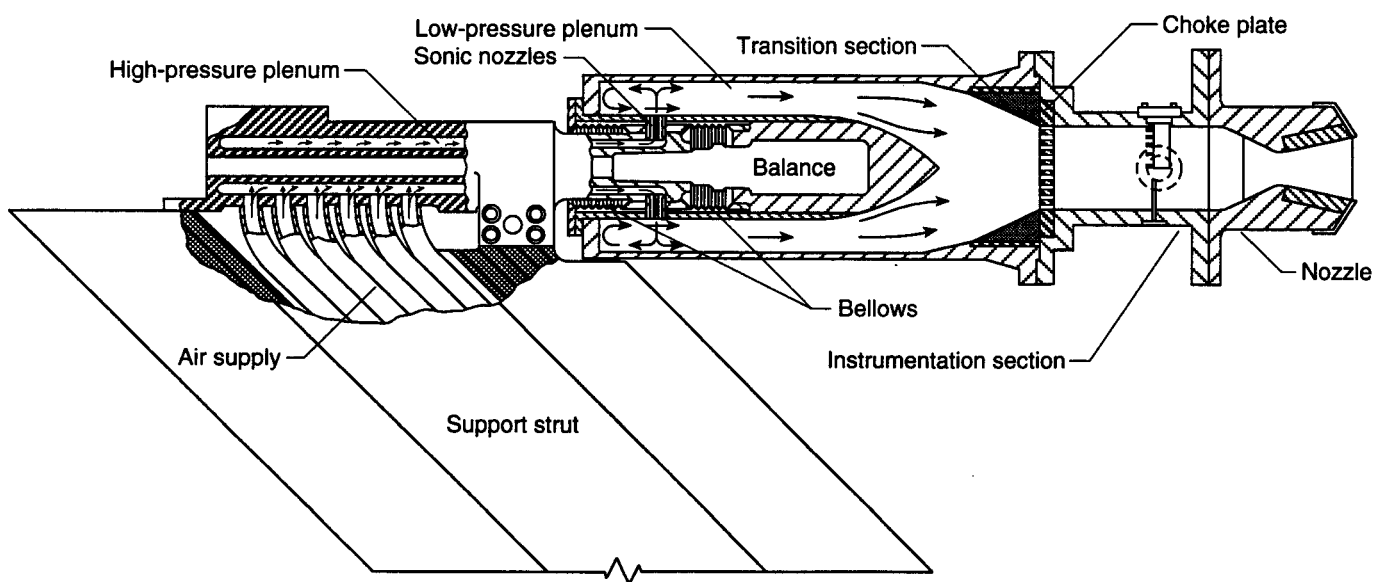
Fig. 6 Sketch of the propulsion simulation system with nozzle model installed.

11
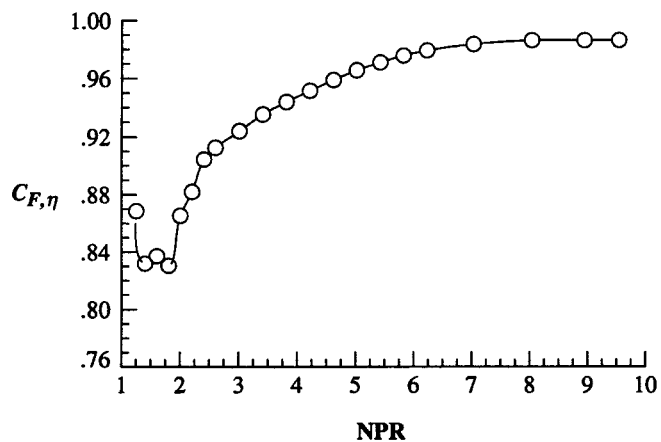
Fig. 7 Nozzle thrust efficiency performance for the baseline configuration.
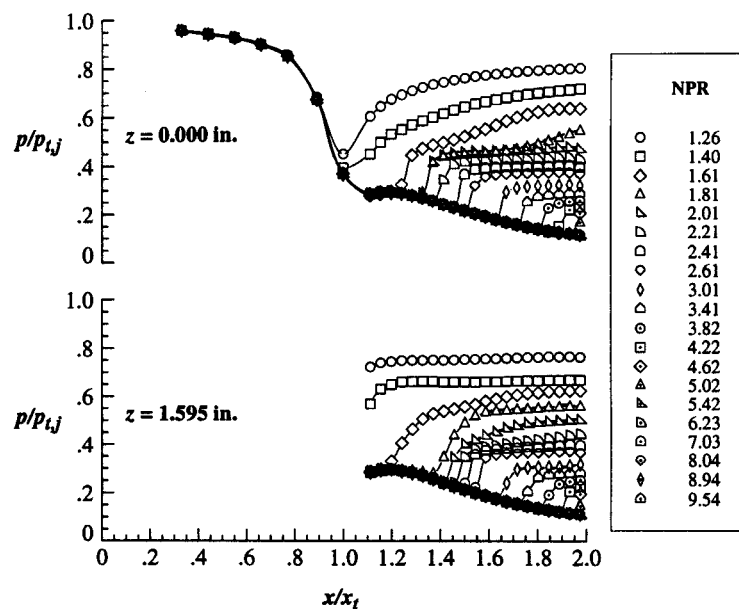
Fig. 8 Internal static pressure distributions for the baseline configuration.
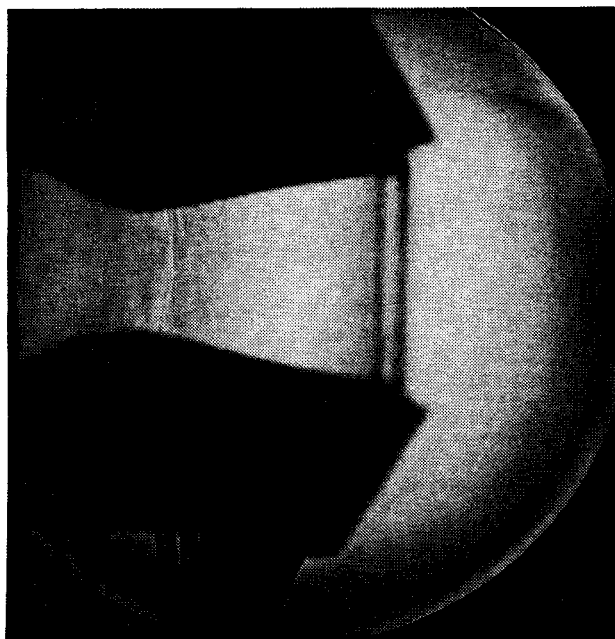
(a) NPR=1.4.
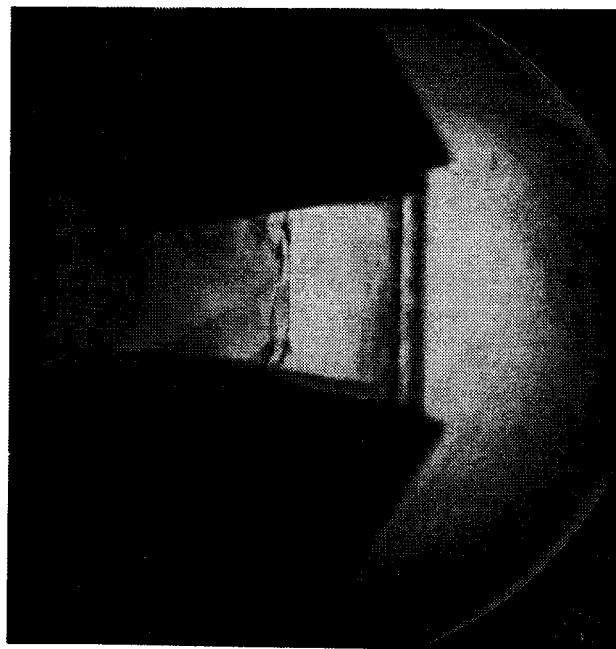
Fig. 9 Focusing schlieren flow visualization for the baseline configuration.

(b) NPR=1.8.
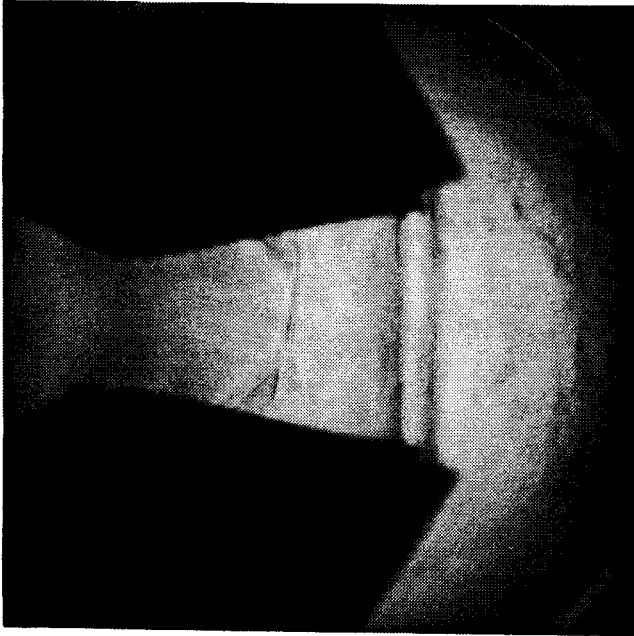
Fig. 9 Continued.

(c) NPR=2.0.

Fig. 9 Concluded.
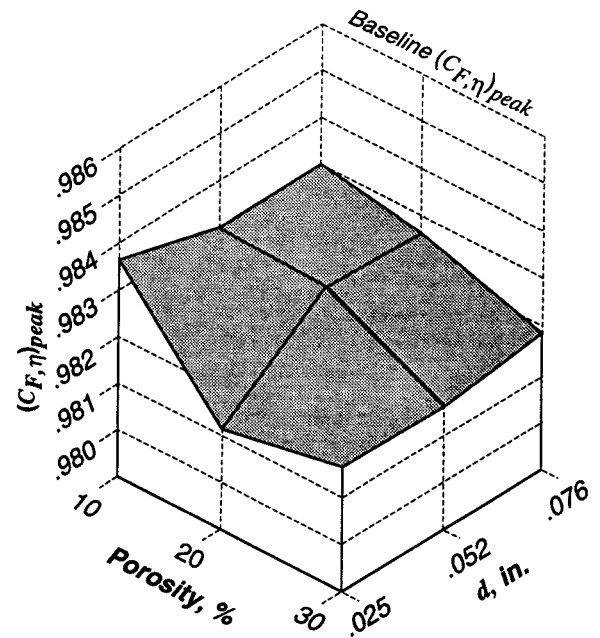
(a) Shallow cavity.

Fig. 10 Effect of percent porosity and hole diameter on peak thrust efficiency.
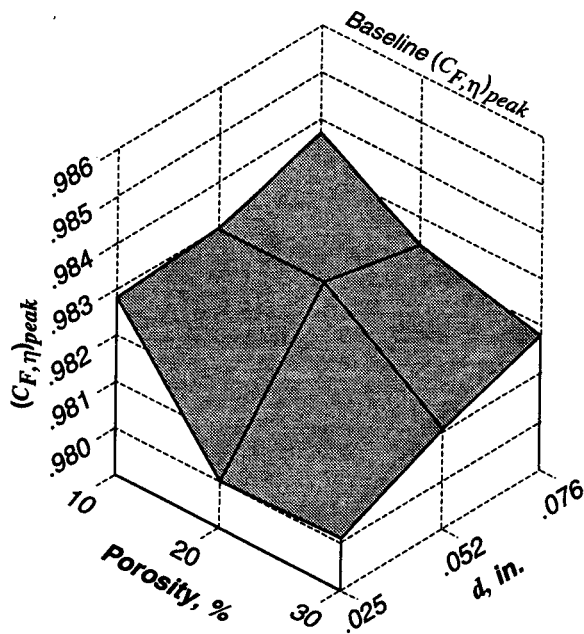
(b) Medium cavity.

Fig. 10 Continued.
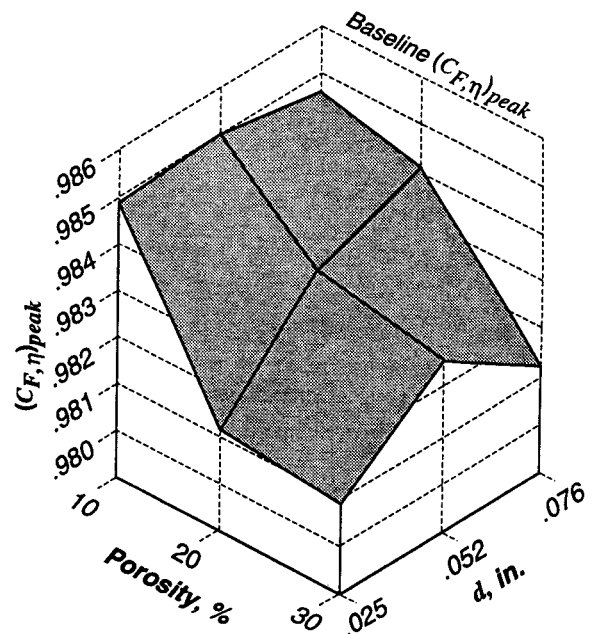
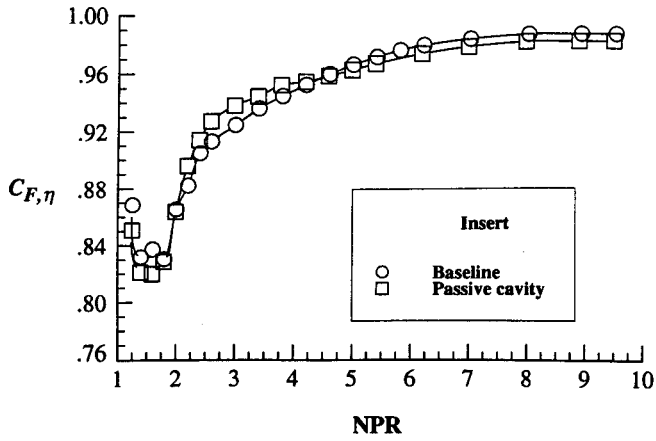(c) Deep cavity.

Fig. 10 Concluded.

13
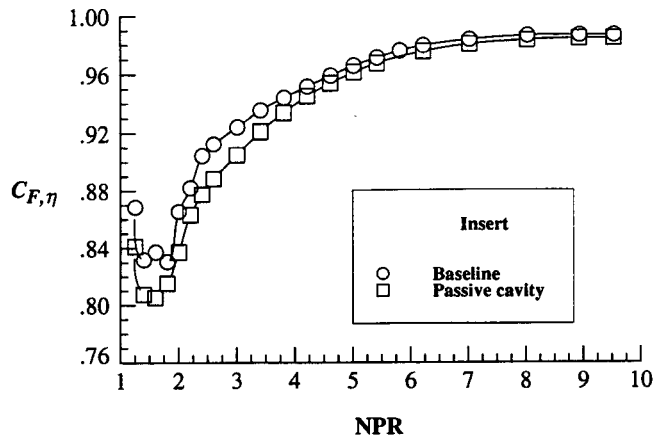
Fig. 11 Nozzle thrust efficiency performance for the baseline configuration and the passive cavity configuration with 10% porosity, d=0.076 in. and deep cavity.
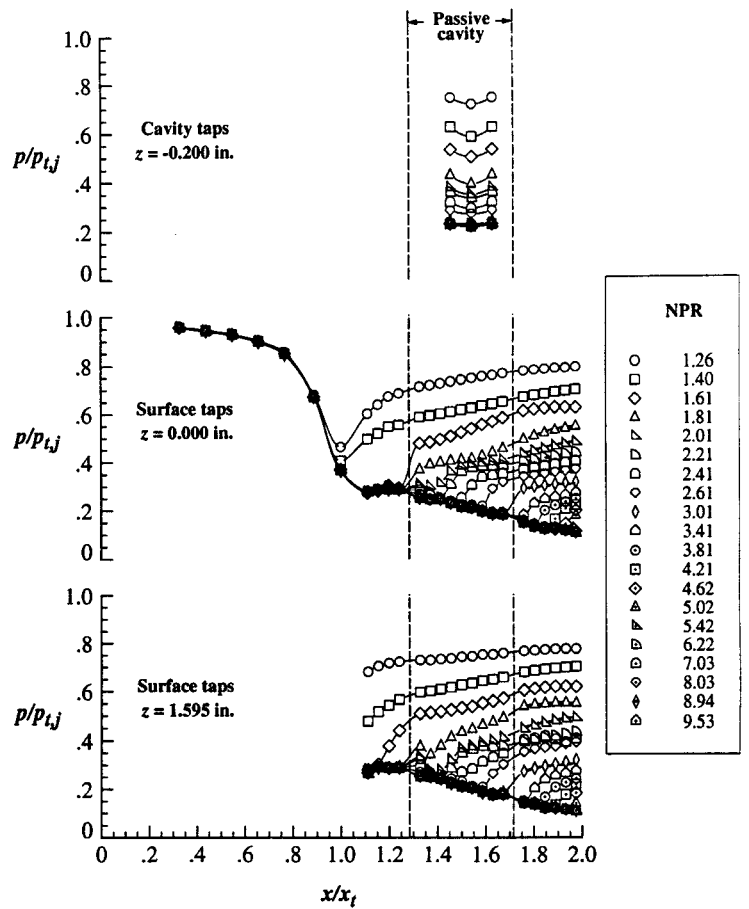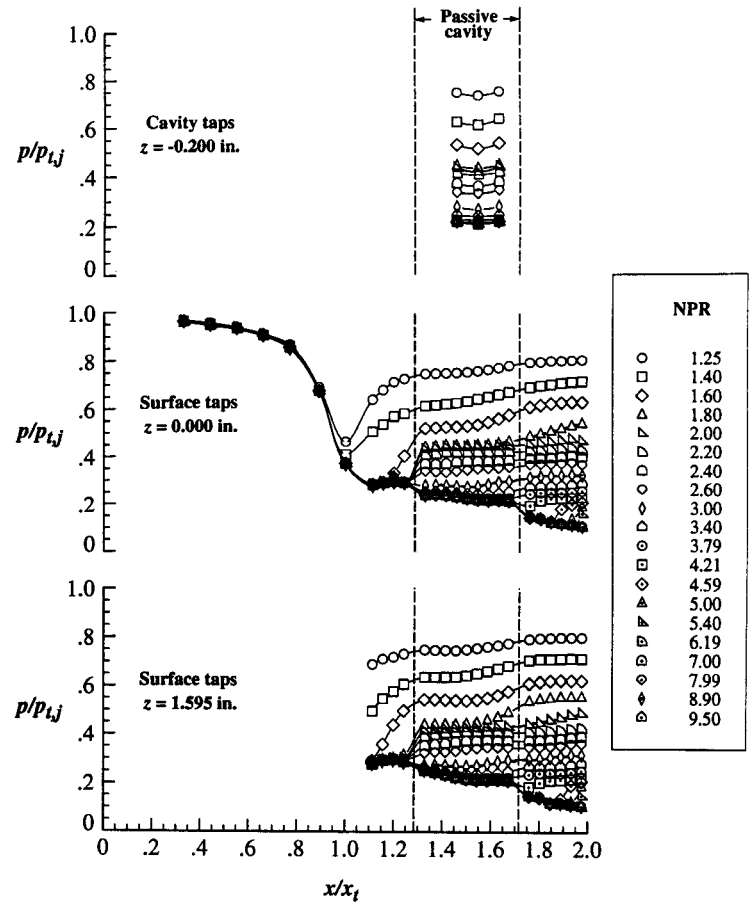

Fig. 12 Internal static pressure distributions for the passive cavity configuration with 10% porosity, d=0.076 in. and deep cavity.
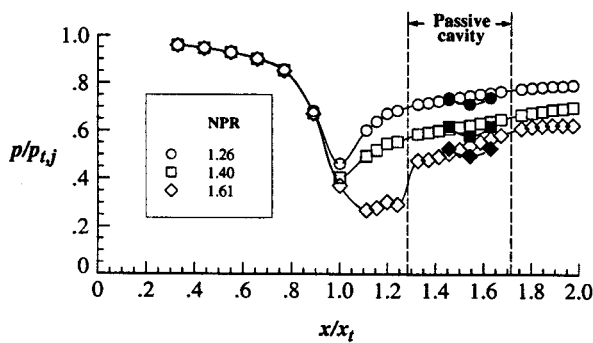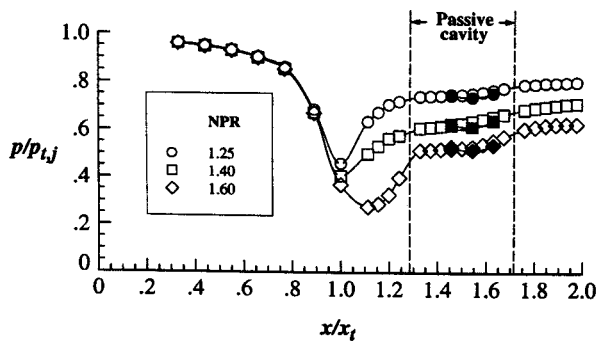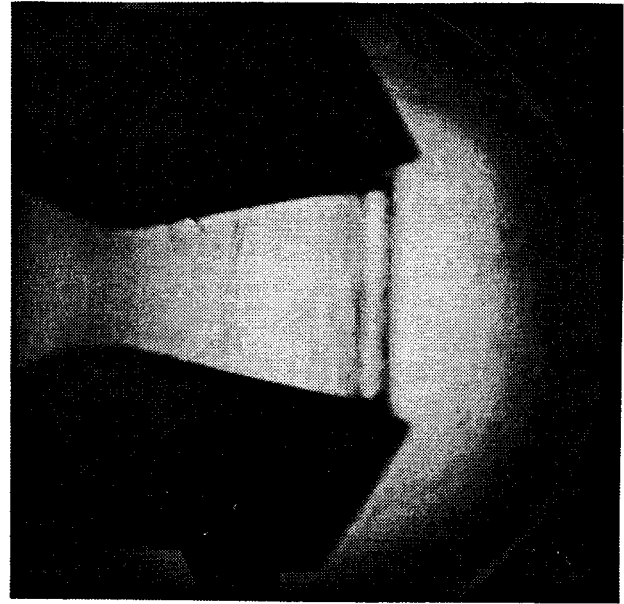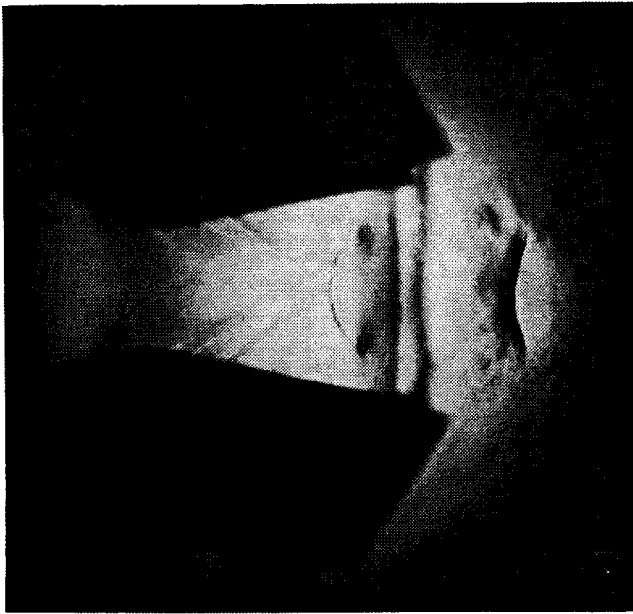

Fig. 13 Centerline surface (open symbols) and cavity (solid symbols) internal static pressure distributions at NPR's from 1.26 to 1.61 for the passive cavity configuration with 10% porosity, d=0.076 in. and deep cavity.
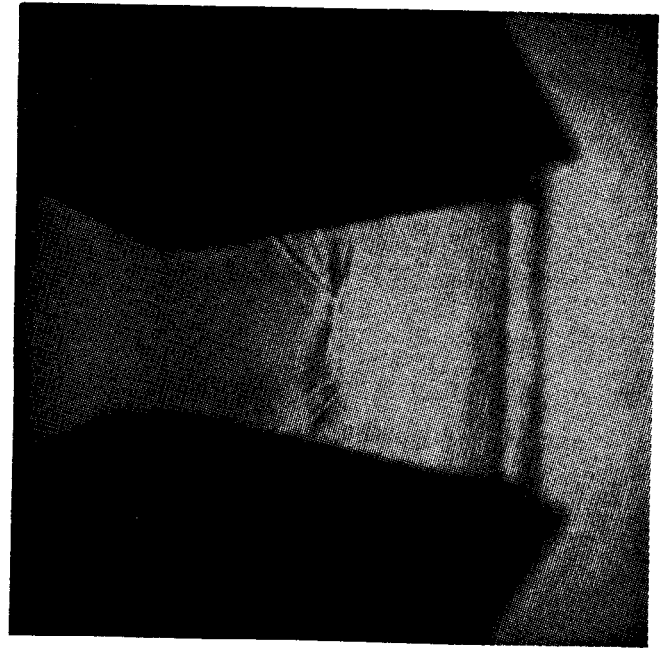
(a) NPR=1.8.

Fig. 14 Focusing schlieren flow visualization for the passive cavity configuration with 10% porosity, d=0.076 in. and deep cavity.
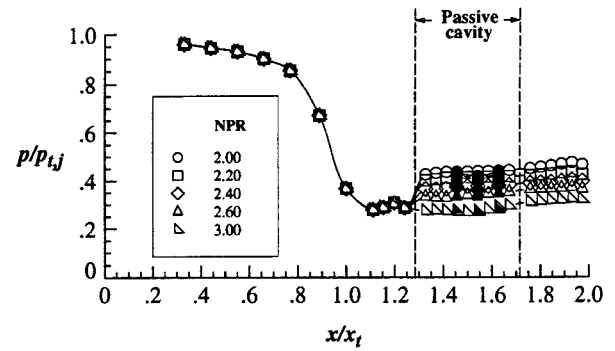
14
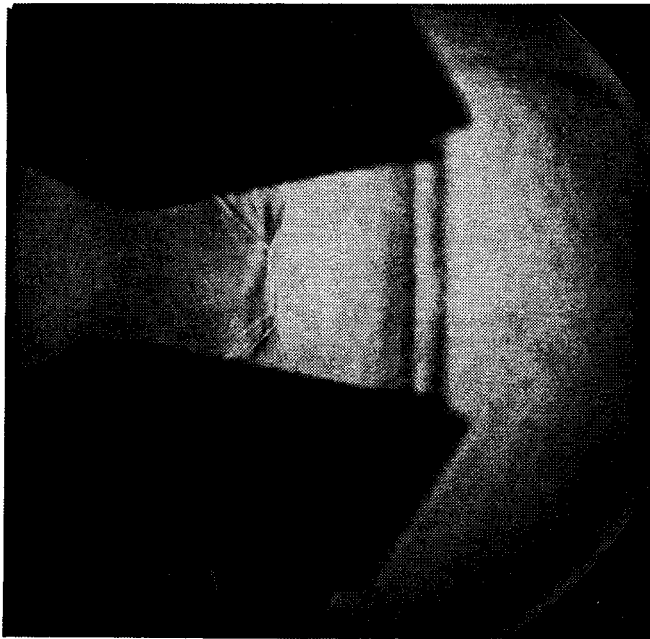
(b) NPR=2.0.

Fig. 14 Concluded.
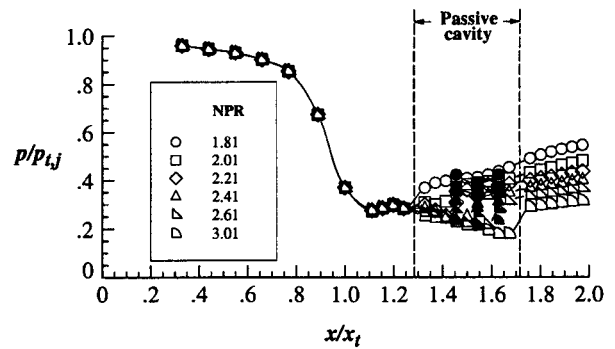
Fig. 15 Centerline surface (open symbols) and cavity (solid symbols) internal static pressure distributions at NPR's from 1.81 to 3.01 for the passive cavity configuration with 10% porosity, d=0.076 in. and deep cavity.
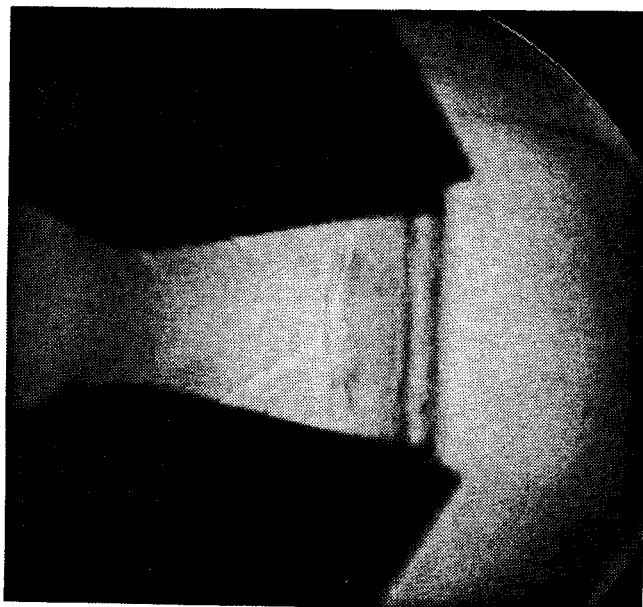
(a) NPR=2.4.
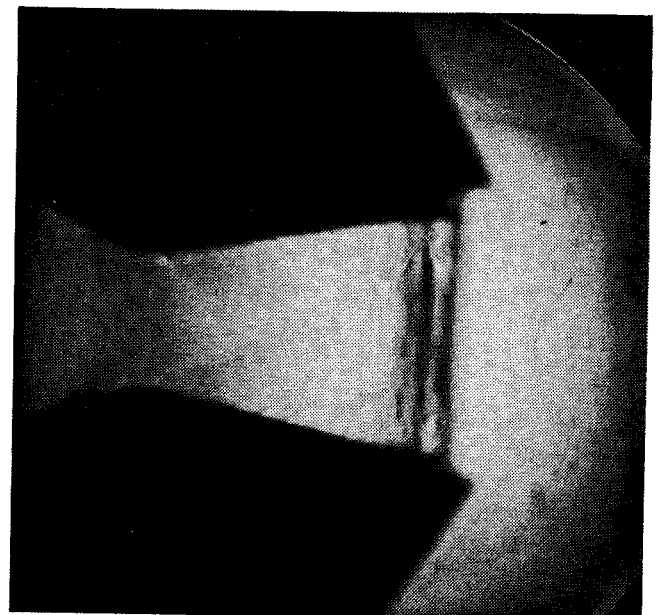
Fig. 16 Focusing schlieren flow visualization at NPR's of 2.4 and 3.0 for the passive cavity configuration with 10% porosity, d=0.076 in. and deep cavity.

(b) NPR=3.0.

Fig. 16 Concluded.

15

Fig. 17 Nozzle thrust efficiency performance for the baseline configuration and the passive cavity configuration with 20% porosity, d=0.025 in. and shallow cavity.

Fig. 18 Internal static pressure distributions for the passive cavity configuration with 20% porosity, d=0.025 in. and shallow cavity.

Fig. 19 Centerline surface (open symbols) and cavity (solid symbols) internal static pressure distributions at NPR's from 1.25 to 1.60 for the passive cavity configuration with 20% porosity, d=0.025 in. and shallow cavity.

(a) NPR=1.8.

Fig. 20 Focusing schlieren flow visualization at NPR's of 1.8 and 2.6 for the passive cavity configuration with 20% porosity, d=0.025 in. and shallow cavity.

16

(b) NPR=2.6.

Fig. 20 Concluded.

Fig. 21 Centerline surface (open symbols) and cavity (solid symbols) internal static pressure distributions at NPR's from 2.00 to 3.00 for the passive cavity configuration with 20% porosity, d=0.025 in. and shallow cavity.
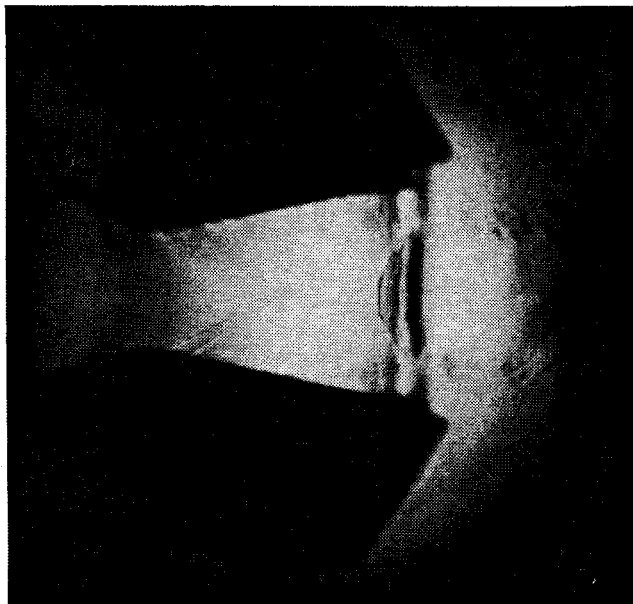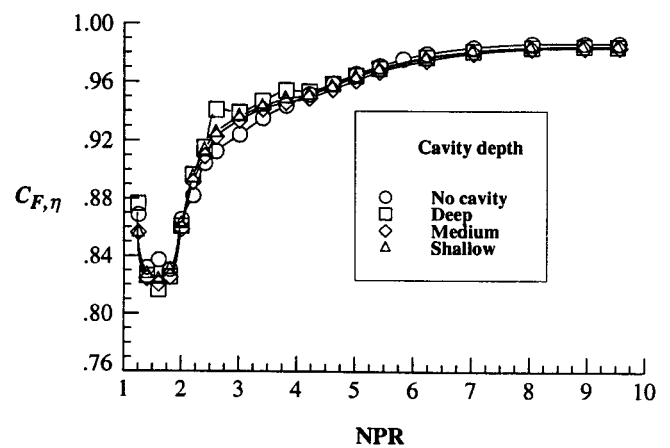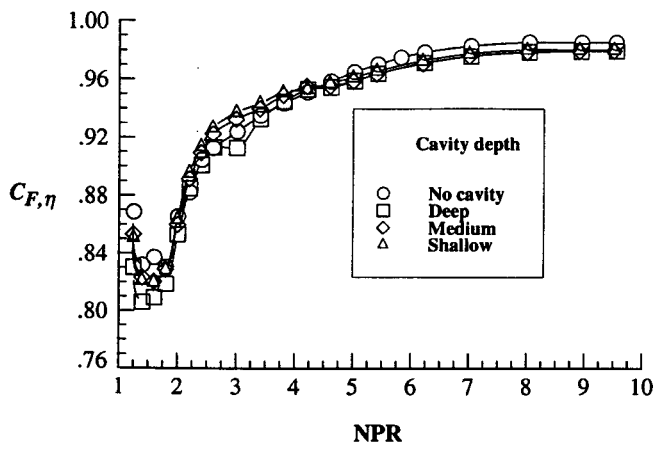

Fig. 22 Focusing schlieren flow visualization at NPR=3.0 for the passive cavity configuration with 20% porosity, d=0.025 in. and shallow cavity.
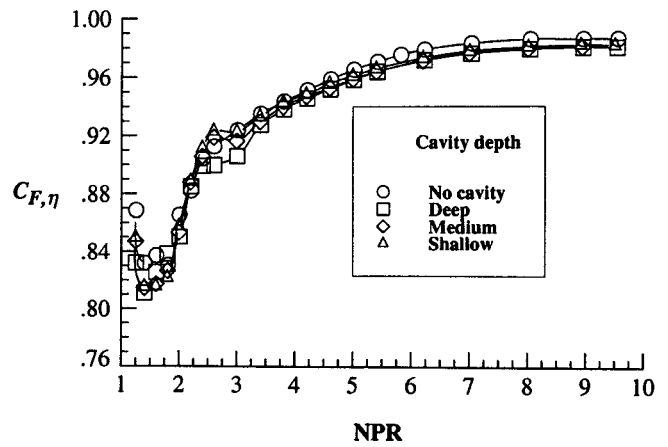
(a) 10% porosity.

Fig. 23 Effect of cavity depth on nozzle thrust efficiency for passive cavity configurations with d=0.025 in.

17

(b) 20% porosity.

Fig. 23 Continued.

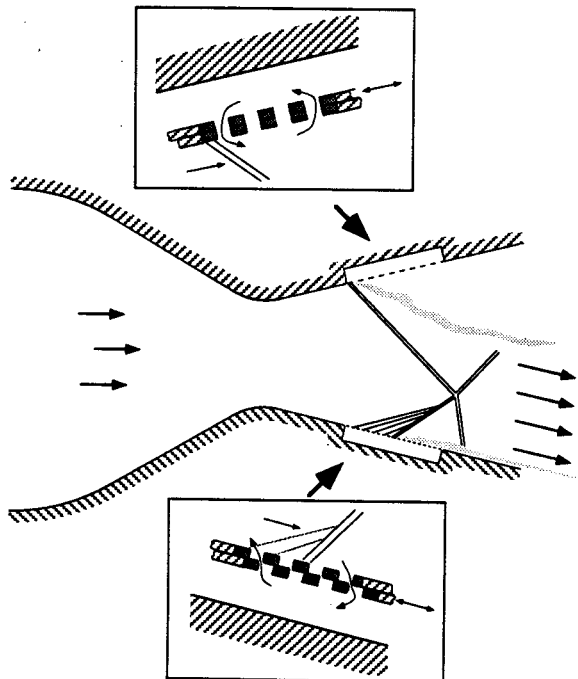(c) 30% porosity.

Fig. 23 Concluded.

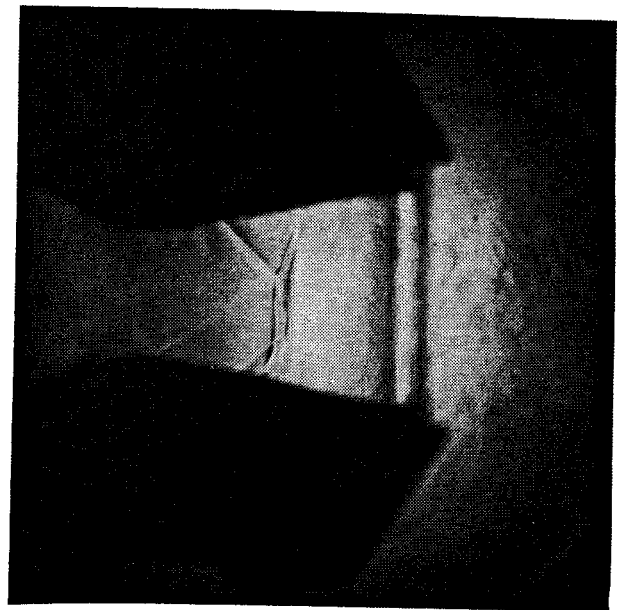Fig. 24 Sketch showing sliding porous plate passive cavity control concept.

Fig. 25. Focusing schlieren flow visualization at NPR=2.0 showing thrust vectoring capability of the passive cavity nozzle concept.

18